



HAL
open science

Phase-field Lattice Boltzmann model for liquid bridges and coalescence in wet granular media

Nabil Younes, Z. Benseghier, O. Millet, A. Wautier, F. Nicot, R. Wan

► **To cite this version:**

Nabil Younes, Z. Benseghier, O. Millet, A. Wautier, F. Nicot, et al.. Phase-field Lattice Boltzmann model for liquid bridges and coalescence in wet granular media. *Powder Technology*, 2022, 411, pp.117942. 10.1016/j.powtec.2022.117942 . hal-03800863

HAL Id: hal-03800863

<https://hal.inrae.fr/hal-03800863>

Submitted on 6 Oct 2022

HAL is a multi-disciplinary open access archive for the deposit and dissemination of scientific research documents, whether they are published or not. The documents may come from teaching and research institutions in France or abroad, or from public or private research centers.

L'archive ouverte pluridisciplinaire **HAL**, est destinée au dépôt et à la diffusion de documents scientifiques de niveau recherche, publiés ou non, émanant des établissements d'enseignement et de recherche français ou étrangers, des laboratoires publics ou privés.

Phase-field Lattice Boltzmann model for liquid bridges and coalescence in wet granular media

N. Younes^{a,b,*}, Z. Benseghier^a, O. Millet^a, A. Wautier^b, F. Nicot^c, R. Wan^d

^a*LaSIE, UMR CNRS 7356, University of La Rochelle, La Rochelle, France*

^b*Aix-Marseille University, INRAE, UMR RECOVER, Aix-en-Provence, France*

^c*University Savoie Mont-Blanc, EDYTEM (USMB/CNRS), Le Bourget du Lac, France*

^d*Department of Civil Engineering, Schulich School of Engineering, University of Calgary, Calgary, Canada*

Abstract

In this paper a phase-field based Lattice Boltzmann model is formulated to simulate the formation and coalescence of capillary bridges between spherical solid particles as well as the associated capillary forces. To capture the air-water interface, Allen-Cahn equation is coupled with two-phase Navier-Stokes equation through a surface tension term. The capillary force arising from the water interaction with a curved solid surface is formulated along with a numerical integration scheme. Two benchmark examples are considered to validate the proposed model, namely: the spreading of a drop on a spherical particle and capillary rise in a narrow tube. Then, the capillary forces due to isolated and coalesced liquid in two and three spherical particle configurations are computed to illustrate the pendular regime and its transition to the funicular regime. Numerical simulation results are found to be in good agreement with available experimental and numerical data for wetting in a doublet and a triplet of particles, respectively. The numerical results indicate that the proposed model provides a viable framework within which the complex capillary interface evolution during the wetting of a large assembly of particles could be captured.

Keywords: capillary bridges, contact angle, multi-phase, LBM, capillary forces, GPU.

*Correspondence:

Email address: nabil.younes@univ-lr.fr (N. Younes)

URL: [orcid.org/ 0000-0003-4431-555X](https://orcid.org/0000-0003-4431-555X) (N. Younes)

1. Introduction

Capillary forces are ubiquitous in many industrial engineering applications, for instance, mixing granular materials (Liu et al., 2013) and powders caking (Hartmann and Palzer, 2011) and many others. Therefore, capillary forces play a crucial role in modifying the behavior of partially saturated granular assemblies (Richefeu et al., 2009; Mielniczuk et al., 2015; Dörmann and Schmid, 2017; Wang et al., 2017a; Louati et al., 2017; Grof et al., 2008). These forces arise when a small quantity of liquid adheres to the grains surfaces, which affects the stability of granular systems at a certain scale. As the liquid content increases until saturation, the capillary cohesion may be lost and the sample may collapse, for instance, the sandcastle (Lu et al., 2007; Hornbaker et al., 1997). Thus, it is necessary to quantify accurately the capillary forces acting within unsaturated granular materials.

Several theoretical and experimental studies have been conducted to calculate capillary forces based on the solution of the Young-Laplace equation in simple axisymmetric configurations. For instance, in Mielniczuk et al. (2018), the capillary forces induced by liquid bridges at the interface of two spherical particles are calculated using an inverse technique to solve Young-Laplace equation when the capillary pressure is unknown (Gagneux and Millet, 2014). This method for calculating the capillary forces was extended to liquid bridges between two different sized spherical particles, between two parallel planes, and between a plane and a spherical particle (Nguyen et al., 2019c,b, 2020a, 2021). Several experimental and theoretical studies have been reported in the literature to study the rupture of capillary bridges due to separation distances between two spherical particles or between spherical particle and a plane (Zhao et al., 2019; Lievano et al., 2017; Wang et al., 2017b). When the separation distance between two spherical particles increases, a rupture of the capillary bridge will take place, and thus the associated capillary force vanishes. They have experimentally and theoretically investigated the rupture of capillary bridges between two or three spherical particles. Moreover, Nguyen et al. (2020b) have developed an original method to measure the surface tension via capillary forces. Furthermore, an experimental and a theoretical studies on the impact of the surface roughness on capillary force between particle-wall collision was conducted by Li et al. (2020). They have revealed that capillary forces increase with the increas-

ing of the surface roughness. In addition, in the case where the pressure is known, the capillary forces can be calculated numerically by solving directly Young-Laplace equation for a symmetrical doublet (Duriez and Wan, 2017). In the case of a more complex configuration (assembly of several particles) or when the symmetry is lost, the above-mentioned analytical methods fail to compute the capillary forces, requiring numerical simulations. Surface energy minimization is one of such numerical methods (Brakke, 1992). In Miot et al. (2021); Wang et al. (2017b), the authors have used this approach combined with the Virtual Work Principle to compute the capillary force induced by liquid bridges between two and three spherical particles. Even though the method can be applied to complex geometrical configurations, it is limited to steady state problems and the convergence of the capillary forces is sensitive to the number of iterations in gradient descent and to re-meshing of the capillary interface (Miot et al., 2021; Di Renzo et al., 2020). Moreover, Wu et al. (2020) have also computed capillary forces for different contact angles of the spherical particles. Rather a good agreement was found between their results and those done experimentally. The biggest drawback of the aforementioned method is that an automatic merging of isolated capillary bridges is impossible to be considered. Instead, contact lines between capillary bridges should manually be detected, and if a contact between them takes place, then a re-meshing must be done. Other methods to address this issue are based on Volume Of Fluid (VOF) approach to track the free surface (Sun and Sakai, 2016), or diffuse interface models (phase-field) to track the interface between liquid-gas phases. These approaches can be combined with Navier-Stokes equations and with immersed-boundary method to compute the capillary forces (Liu et al., 2017; Liu and Ding, 2015). However, these methods are not easy to implement and computationally expensive as they are hardly parallelizable.

Alternatively, the diffuse interface models and the Navier-Stokes equations can be solved using the Lattice Boltzmann method to simulate gas-liquid-solid flow accounting for the liquid-solid wetting behaviour. The Lattice Boltzmann method has the benefit of dealing with complex geometry. Moreover, it is amenable to parallelization, especially when using Graphics Processor Unit (GPU) computational architecture. Zhang et al. (2020) recently developed an accurate method to calculate the capillary force for moving particles in 2D.

This paper aims at implementing the phase-field model, developed by Liang et al. (2018, 2019); Benseghier et al. (2021), that involves the conservative

Allen–Cahn equation coupled with Navier–Stokes equations. This enables us to achieve a high-density ratio between liquid and gas and to calculate very accurately the capillary forces. The implementation is validated by comparing experimental and numerical results in the literature, for capillary bridge formation between two and three spherical particles, including coalescence of capillary bridges.

This paper is organized as follows. First, the phase-field theory for multi-phase flow is presented with the associated Boundary Conditions (BCs), i.e. non-slip and wetting BC. The next section is devoted to benchmark simulations to validate the wetting condition and the overall numerical implementation. Two benchmark simulations are performed: spreading of a drop on a spherical particle, and capillary rise in a narrow tube. Next, a section is dedicated to the numerical calculation of capillary forces. Then, the capillary force implementation is validated from the example of an axisymmetric capillary bridge between two particles and the comparison with the experimental and numerical results of [Mielniczuk et al. \(2018\)](#) and [Miot et al. \(2021\)](#), respectively. The second validation example consists of an assembly of three particles with two capillary doublets, and two different regimes from un-coalesced to coalesced bridges. We recover the theoretical and the simulation results of [Miot et al. \(2021\)](#) with a sudden increase of the capillary forces at coalescence. Finally, the last section provides a general conclusion and perspectives for future investigations.

2. Numerical models

In order to model partially saturated granular materials, there is a need to use a numerical method taking into account both the fluid (liquid and gas) and the interface (gas/liquid) behaviors. If we assume that the interface is diffuse, phase-field based models can be used solving Navier–Stokes Equation (NSE) coupled with Cahn–Hilliard or Allen–Cahn equations in an LBM framework ([Fakhari and Rahimian, 2010](#); [Fakhari and Lee, 2013](#); [Fakhari et al., 2017a,b](#); [Wang et al., 2016](#); [Krueger et al., 2016](#); [Zheng et al., 2015](#); [He et al., 2019](#); [Wang et al., 2019](#); [Huang et al., 2009](#); [Stratford et al., 2005](#)). Cahn–Hilliard and Allen–Cahn equations describe the evolution of the phase field $\phi(\mathbf{x}, t)$ which is equal to 1 in the liquid, 0 in the gas, and $\phi \in]0; 1[$ in the interface. The asset of this method is the natural tracking of the interface by solving one of the aforementioned equations. Compared to Cahn–Hilliard equation, conservative Allen–Cahn Equation (ACE) preserves the mass in numerical

integration (Liang et al., 2018, 2019). Accordingly, ACE coupled with NSE are selected for this study.

2.1. Allen-Cahn and Navier-Stokes equations

The moving interface between two phases (e.g. water and air), advected by the fluid velocity \mathbf{u} , can be modelled using the conservative Allen-Cahn equation (also known as the conservative phase-field equation) (Chiu and Lin, 2011; Sun and Beckermann, 2007)

$$\frac{\partial \phi}{\partial t} + \nabla \cdot (\phi \mathbf{u}) = \nabla \cdot [M(\nabla \phi - \lambda \mathbf{n})] \quad (1)$$

where $\phi(\mathbf{x}, t)$ is the phase-field parameter used to identify the regions occupied by the two fluids. This parameter takes the value 1 in the liquid phase, 0 in the gas phase, and between 0 and 1 in the interface as indicated in Fig. 1b. Once $\phi(\mathbf{x}, t)$ is determined, the fluid density ρ is computed as follows

$$\rho(\mathbf{x}, t) = \phi(\rho_l - \rho_g) + \rho_g \quad (2)$$

where ρ_l and ρ_g are liquid and gas densities far from the interface, assumed to be constant.

In Eq. (1), M denotes the mobility and \mathbf{n} is the unit normal vector to the interface defined as:

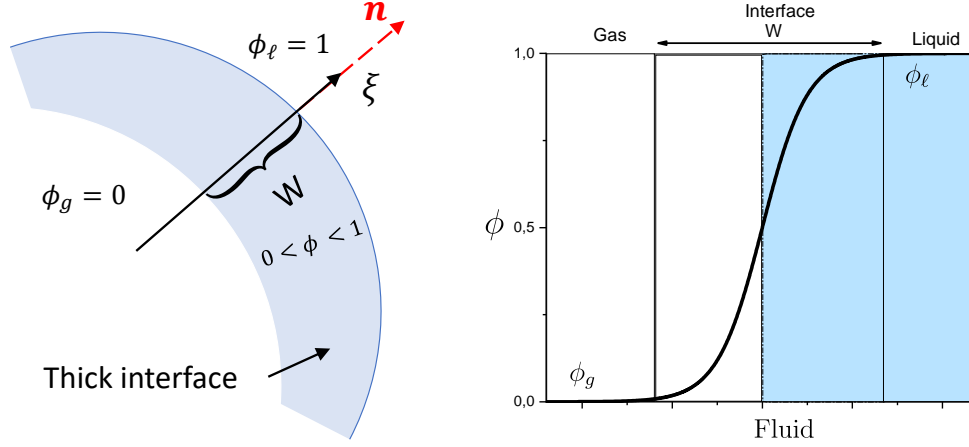
$$\mathbf{n} = \frac{\nabla \phi}{|\nabla \phi|}. \quad (3)$$

For numerical stability, it is convenient to model the interface as a regularized surface of thickness W as illustrated in Fig. 1a instead of a sharp one. Accordingly, the evolution of $\phi(\mathbf{x}, t)$ crossing the interface should be regularized as well, such as using a hyperbolic tangent function instead of a Heaviside function¹. In order to find the regularized function crossing the interface, we recall the formula of the mixing energy $F(\phi, \nabla \phi)$, whose expression (see for instance Penrose and Fife (1990)) is

$$F(\phi, \nabla \phi) = \int_{\Omega} \left[\psi(\phi) + \frac{k}{2} |\nabla \phi|^2 \right] dx \quad (4)$$

where Ω is the physical domain occupied by the matter and $\psi(\phi) = \beta \phi^2 (\phi - 1)^2$ is the free-energy density (Jacqmin, 1999; Lee and Kim, 2012). The

¹The Heaviside function is usually used to brutally separate two phases.



(a) Scheme describing the interface.

(b) Evolution of ϕ through the interface.

Figure 1: Presentation of concepts and phenomena related to the interface.

parameters k and β depend on the surface tension γ and on the interface thickness W , through the following relations:

$$k = \frac{3}{2}\gamma W; \beta = \frac{12\gamma}{W}. \quad (5)$$

The chemical potential μ_ϕ is defined as the minimum of the mixing energy $F(\phi, \nabla\phi)$; thus μ_ϕ satisfies:

$$\mu_\phi = \frac{\delta F}{\delta\phi} = \frac{\partial F}{\partial\phi} - \nabla \cdot \left(\frac{\partial F}{\partial\nabla\phi} \right) = \frac{\partial\psi}{\partial\phi} - k\nabla^2\phi = 4\beta\phi(\phi - 1) \left(\phi - \frac{1}{2} \right) - k\nabla^2\phi. \quad (6)$$

The regularized interface evolution ϕ_{eq} is defined at thermodynamic equilibrium when the μ_ϕ is nil. If we express ϕ_{eq} in terms of the interface normal local system ξ as indicated in Fig. 1a, $\nabla^2\phi$ becomes then $\phi''(\xi)$. Consequently, after substitutions, and at the thermodynamic equilibrium, Eq. (6) yields:

$$\mu_\phi = 4\beta\phi_{\text{eq}}(\xi) [\phi_{\text{eq}}(\xi) - 1] \left[\phi_{\text{eq}}(\xi) - \frac{1}{2} \right] - k\phi_{\text{eq}}''(\xi) = 0. \quad (7)$$

After solving the above differential equation, ϕ_{eq} can be expressed as:

$$\phi_{\text{eq}}(\xi) = \frac{1}{2} + \frac{1}{2} \tanh \left(\frac{2\xi}{W} \right). \quad (8)$$

Therefore, the regularized interface is simply defined as a hyperbolic tangent function as depicted in Fig. 1b.

Moreover, the parameter λ , from the right hand side of Allen-Cahn equation (1), is the norm of gradient vector of ϕ_{eq} at equilibrium which can be expressed as:

$$\lambda = |\nabla\phi|_{\text{eq}} = \frac{d\phi_{\text{eq}}}{d\xi} = \frac{4\phi(1-\phi)}{W}. \quad (9)$$

For incompressible two-phase flows, the modified Navier-Stokes equations may be written as

$$\rho \left(\frac{\partial \mathbf{u}}{\partial t} + \mathbf{u} \cdot \nabla \mathbf{u} \right) = -\nabla p + \nabla \cdot [\rho \nu (\nabla \mathbf{u} + \nabla \mathbf{u}^T)] + \mathbf{F}_s + \mathbf{G} \quad (10)$$

$$\nabla \cdot \mathbf{u} = 0$$

where \mathbf{u} is the fluid velocity, ν is the kinematic viscosity, p is the hydrodynamic pressure, \mathbf{G} is the body force, and \mathbf{F}_s is the surface tension force. In Eq. (10), the coupling with Allen-Cahn equation is included in the definition of the surface tension term \mathbf{F}_s as in Liang et al. (2018); Li et al. (2019); Fakhari and Bolster (2017); Benseghier et al. (2021):

$$\mathbf{F}_s = \mu_\phi \nabla \phi. \quad (11)$$

It is worth mentioning that the coupling is also done via the fluid density ρ which depends on ϕ as already seen in Eq. (2).

2.2. Associated Lattice-Boltzmann models

The LB models for solving the conservative Allen-Cahn Equation (ACE) (1) and Navier-Stokes Equations (NSE) (10) rely on two families of particle distribution functions $g_\alpha(\mathbf{x}, t)$ and $f_\alpha(\mathbf{x}, t)$ related to the ACE and NSE, respectively. Their spatio-temporal evolution is described with Bhatnagar-Gross-Krook (BGK) collision operator based on the discretization method proposed in Liang et al. (2018, 2019); Benseghier et al. (2021)

$$g_\alpha(\mathbf{x} + \mathbf{c}_\alpha \Delta t, t + \Delta t) = g_\alpha(\mathbf{x}, t) - \frac{1}{\tau_g} [g_\alpha(\mathbf{x}, t) - g_\alpha^{eq}(\mathbf{x}, t)] + \Delta t G_\alpha(\mathbf{x}, t) \quad (12)$$

$$f_\alpha(\mathbf{x} + \mathbf{c}_\alpha \Delta t, t + \Delta t) = f_\alpha(\mathbf{x}, t) - \frac{1}{\tau_f} [f_\alpha(\mathbf{x}, t) - f_\alpha^{eq}(\mathbf{x}, t)] + \Delta t F_\alpha(\mathbf{x}, t) \quad (13)$$

where τ_g and τ_f are the non-dimensional relaxation times for $g(\mathbf{x}, t)$ and $f(\mathbf{x}, t)$ probability density functions respectively. $G_\alpha(\mathbf{x}, t)$ and $F_\alpha(\mathbf{x}, t)$ are the source terms. Finally, $g_\alpha^{eq}(\mathbf{x}, t)$ and $f_\alpha^{eq}(\mathbf{x}, t)$ are the equilibrium distribution functions given by:

$$g_\alpha^{eq}(\mathbf{x}, t) = \omega_\alpha \phi \left(1 + \frac{\mathbf{c}_\alpha \cdot \mathbf{u}}{c_s^2} \right) \quad (14)$$

$$f_\alpha^{eq} = \begin{cases} \frac{p}{c_s^2}(\omega_\alpha - 1) + \rho s_\alpha(\mathbf{u}), & \alpha = 0 \\ \frac{p}{c_s^2}\omega_\alpha + \rho s_\alpha(\mathbf{u}), & \alpha \neq 0 \end{cases} \quad (15)$$

with

$$s_\alpha(\mathbf{u}) = \omega_\alpha \left[\frac{\mathbf{c}_\alpha \cdot \mathbf{u}}{c_s^2} + \frac{(\mathbf{c}_\alpha \cdot \mathbf{u})^2}{2c_s^4} - \frac{\mathbf{u} \cdot \mathbf{u}}{2c_s^2} \right] \quad (16)$$

where $\mathbf{u} = \mathbf{u}(\mathbf{x}, t)$ is the fluid velocity, ρ is the density, and p is the pressure. The phase-field ϕ parameter is computed from the distribution function g_α as:

$$\phi = \sum_{\alpha} g_\alpha. \quad (17)$$

The macroscopic quantities \mathbf{u} and p can be calculated as follows (Liang et al., 2018, 2019; Benseghier et al., 2021):

$$\rho \mathbf{u} = \sum_{\alpha} \mathbf{c}_\alpha f_\alpha + \frac{\Delta t}{2} (\mu_\phi \nabla \phi + \mathbf{G}) \quad (18)$$

$$p = \frac{c_s^2}{(1 - \omega_0)} \left[\sum_{\alpha \neq 0} f_\alpha + \frac{\Delta t}{2} (\rho_l - \rho_g) \mathbf{u} \cdot \nabla \phi + \rho s_0(\mathbf{u}) \right]. \quad (19)$$

In Eqs. (14) and (15), $c_s = c/\sqrt{3}$ is the lattice speed of sound for D2Q9, D3Q15, and D3Q19 for discretization schemes. For D3Q7, we have $c_s = c/\sqrt{4}$. The characteristic velocity c is defined classically as $c = \Delta x/\Delta t$, where Δx and Δt denote the lattice size and time step (which are equal to one in lattice units). Furthermore, \mathbf{c}_α are the discrete velocities, which depend on the discretization scheme. In lattice units, the discrete velocities for D3Q19 scheme are

$$\mathbf{c}_\alpha = \begin{cases} (0, 0, 0) & \alpha = 0 \\ (\pm 1, 0, 0), (0, \pm 1, 0), (0, 0, \pm 1), & \alpha = 1, 2, \dots, 6 \\ (\pm 1, \pm 1, 0), (\pm 1, 0, \pm 1), (0, \pm 1, \pm 1) & \alpha = 7, 8, \dots, 18 \end{cases} \quad (20)$$

with the corresponding weights $w_0 = 1/3$, $w_{1-6} = 1/18$ and $w_{7-18} = 1/36$. The source terms G_α and F_α in Eqs. (12) and (13) are defined as in Liang et al. (2018) by

$$G_\alpha = \left(1 - \frac{\Delta t}{2\tau_g}\right) \frac{\omega_\alpha \mathbf{c}_\alpha \cdot [\partial_t(\phi \mathbf{u}) + c_s^2 \lambda \mathbf{n}]}{c_s^2}. \quad (21)$$

$$F_\alpha = \left(1 - \frac{\Delta t}{2\tau_f}\right) \omega_\alpha \left(\frac{\mathbf{c}_\alpha \cdot \mathbf{F}}{c_s^2} + \frac{\mathbf{u} \nabla \rho : \mathbf{c}_\alpha \mathbf{c}_\alpha}{c_s^2} \right) \quad (22)$$

where \mathbf{F} is the total body force, including the surface tension body force \mathbf{F}_s , according to Eq. (11), and the external body force \mathbf{G} :

$$\mathbf{F} = \mathbf{F}_s + \mathbf{G}. \quad (23)$$

Substituting Eqs. (11) and (2) into Eq. (22), yields:

$$F_\alpha = \left(1 - \frac{\Delta t}{2\tau_f}\right) \omega_\alpha \left(\frac{\mathbf{c}_\alpha \cdot (\mu_\phi \nabla \phi + \mathbf{G})}{c_s^2} + \frac{(\rho_l - \rho_g) \mathbf{u} \nabla \phi : \mathbf{c}_\alpha \mathbf{c}_\alpha}{c_s^2} \right). \quad (24)$$

The mobility M in the ACE is related to the relaxation time τ_g as Liang et al. (2018)

$$M = c_s^2 \left(\tau_g - \frac{\Delta t}{2} \right) \quad (25)$$

and the kinematic viscosity ν is linked to the relaxation time τ_f as:

$$\nu = c_s^2 \left(\tau_f - \frac{\Delta t}{2} \right). \quad (26)$$

It is worth mentioning that the τ_f used in Eqs. (24) and (13) is computed as a linear interpolation depending on the state of a given node in the domain—liquid, gas or interface:

$$\tau_f = \phi (\tau_f^\ell - \tau_f^g) + \tau_f^g \quad (27)$$

As it will be discussed later in the paper, in this study, the transition between initial and equilibrium states is not taken into consideration, thus, viscosities have no influence on the computations during this phase. Consequently, it will be assumed that $\nu^\ell = \nu^g$ which yields to $\tau_f^\ell = \tau_f^g = \tau_f$. The selected

value of τ_f in this paper is $\tau_f = 1$ for numerical stability².

Finally, an explicit Euler scheme is used to compute the temporal derivative in Eq. (21):

$$\partial_t(\phi\mathbf{u}) = [\phi(t)\mathbf{u}(t) - \phi(t - \Delta t)\mathbf{u}(t - \Delta t)] / \Delta t. \quad (28)$$

The second-order isotropic central schemes are applied for the evaluation of gradient and Laplacian operators (Liang et al., 2018):

$$\nabla\phi(\mathbf{x}) = \sum_{\alpha \neq 0} \frac{\omega_\alpha \mathbf{c}_\alpha \phi(\mathbf{x} + \mathbf{c}_\alpha \Delta t)}{c_s^2 \Delta t} \quad (29)$$

$$\nabla^2\phi(\mathbf{x}) = \sum_{\alpha \neq 0} \frac{2\omega_\alpha [\phi(\mathbf{x} + \mathbf{c}_\alpha \Delta t) - \phi(\mathbf{x})]}{c_s^2 \Delta t^2}. \quad (30)$$

2.3. Boundary Conditions (BCs)

2.3.1. Wetting condition

Wettability is defined as the ability of a liquid to keep in contact with a solid surface. For instance, when a liquid droplet comes into contact with a solid surface, a thermodynamic equilibrium between tri-phase matters—liquid, gas, and solid—takes place. The droplet would then spread out—if the contact angle $\theta = 0^\circ$ —or would become a spherical cap if $\theta > 0^\circ$.

Numerically speaking, the wetting condition is ensured based on the cubic BC proposed by Lee and Liu (2010):

$$\mathbf{n}_w \cdot \nabla\phi|_{x_w} = -\sqrt{\frac{2\beta}{k}} \cos\theta (\phi_w - \phi_w^2) \quad (31)$$

where β , k are defined in Eq. (5), and ϕ_w is the value of ϕ at the wall³.

$\mathbf{n}_w \cdot \nabla\phi|_{x_w}$ corresponds to the derivative of ϕ along direction \mathbf{n}_w . Consequently, Eq. (31) is discretized using a centered difference scheme. For a boundary solid node (i, j, k) we have

$$\mathbf{n}_w \cdot \nabla\phi|_{x_w} = \frac{\phi_p - \phi_{(i,j,k)}}{2h} \quad (32)$$

²Viscosity in Eq. (26) must be positive, therefore $\tau_f^{g,\ell} \geq 0.5$ is the only condition for selecting the relaxation time

³Or even spherical obstacle

where h is the distance from the solid node (i, j, k) to the solid surface and ϕ_p is the interpolated value of ϕ at the fluid node located at a distance h from the solid surface (see Fig. 2). ϕ_p is determined using a trilinear interpolation between the adjacent nodes in a cubic lattice 3D conditions. The value of ϕ on the solid interface is then approximated as:

$$\phi_w = \frac{\phi_{(i,j,k)} + \phi_p}{2}. \quad (33)$$

Combining Eqs. (31), (32) and (33) lead to

$$\begin{cases} \phi_{(i,j,k)} = \frac{1}{a} \left(1 + a \pm \sqrt{(1+a)^2 - 4a\phi_p} \right) - \phi_p, & a = hq \neq 0 \quad (\theta \neq 90^\circ) \\ \phi_{(i,j,k)} = \phi_p & (\theta = 90^\circ) \end{cases} \quad (34)$$

with $a = -h\sqrt{\frac{2\beta}{k}} \cos \theta$. In practice, h is usually approximated to half $h = \frac{1}{2}$ in lattice units. Note that for $\theta \neq 90^\circ$, there are two solutions, but only the one that ranges between 0 and 1 is selected.

2.3.2. Non-slip boundary condition

The non-slip boundary condition is ensured by applying the halfway bounce-back scheme at fluid boundary nodes \mathbf{x}_b whose unknown distribution functions f and g are replaced by the ones in the opposite directions:

$$f_{\bar{\alpha}}(\mathbf{x}_b, t + \Delta t) = f_{\alpha}^*(\mathbf{x}_b, t) \quad (35)$$

$$g_{\bar{\alpha}}(\mathbf{x}_b, t + \Delta t) = g_{\alpha}^*(\mathbf{x}_b, t) \quad (36)$$

where $\bar{\alpha}$ stands for the opposite direction of α , f_{α}^* and g_{α}^* are the post-collision distribution functions.

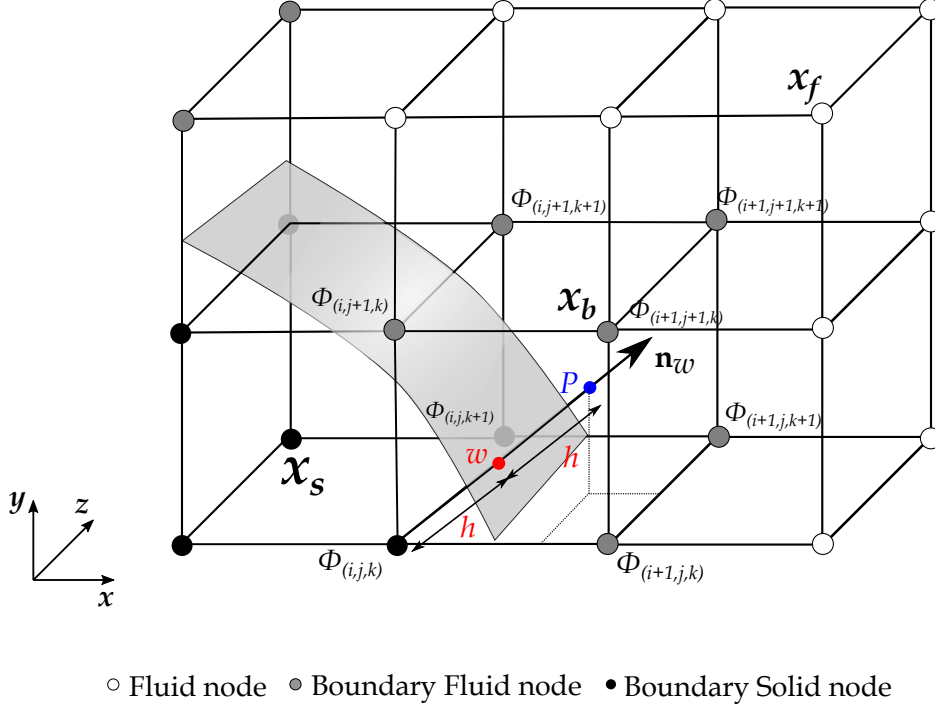


Figure 2: Schematic depicting the geometric parameters for applying the wetting condition. \mathbf{n}_w is the normal unit vector pointing away from the solid wall to the fluid. A tri-linear interpolation is used to obtain the unknown phase value ϕ_p between the 8 adjacent nodes in a cubic lattice.

3. Benchmark simulations

Following the presentation of the aforementioned models and the boundary conditions, the validation phase will be carried out. Two benchmark examples will be performed to check the reliability of the proposed models in order to investigate more complex problems, e.g. capillary bridges and associated capillary forces.

3.1. Drop on a convex spherical surface

A drop on a spherical particle is simulated in order to validate the wetting boundary condition model (31). A water droplet with a radius $r_0 = 20 \text{ lu}^4$

⁴lu denotes lattice unit, c.f. [Appendix A](#) for more details.

is placed at the top of the particle with a radius $R = 60$ lu. The mesh size is $(256 \times 256 \times 256)$. The simulation parameters are $\gamma = 0.2$ lu, $W = 5$ lu, $\rho_l = 1000$ lu, $\rho_g = 1$ lu, and $M = 0.1$ lu. Periodic BCs are applied in all directions. For the solid boundary nodes, we apply the wetting boundary condition Eq. (34) and the bounce-back scheme as shown in Eqs. (35) and (36).

Fig. 3 shows the shapes of the droplet at equilibrium for different imposed contact angles. To measure the effective contact angle, the generalized Pythagorean theorem is used, i.e.

$$\varphi = \arccos \left(\frac{R^2 + r^2 - d^2}{2rR} \right) \quad (37)$$

where r is the drop radius at equilibrium⁵, R is the particle radius, d is the distance between the center of the drop and the particle as shown in Fig. 4.

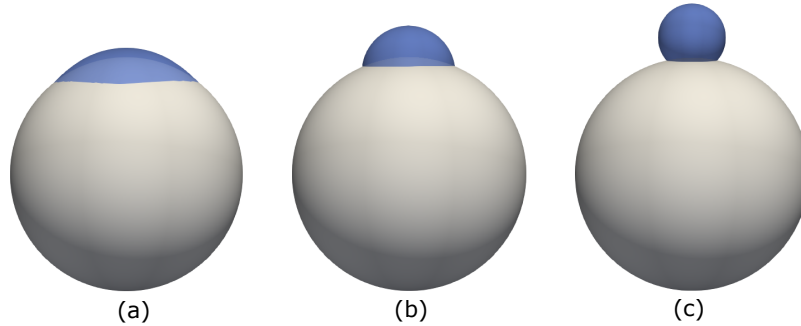


Figure 3: Droplet shape at equilibrium at different imposed contact angles for a drop on a sphere. (a) $\theta = 10^\circ$ (b) $\theta = 60^\circ$, (c) $\theta = 120^\circ$.

The geometric parameters d and r are determined using an image processing in-house *Matlab* code (Benseghier et al., 2021; Nguyen et al., 2019d,a, 2020a). Fig. 5 compares the measured φ and imposed contact angles θ , which validates the interpretation of θ as a contact angle in Eq. (31) (φ and θ coincide). It is worthy to note that for low values of the imposed contact angle, e.g. $\theta = 10^\circ$, numerical noise is observed as shown in Fig. 4. As such, one may notice in Fig. 3 that for $\theta = 10^\circ$, the droplet shape is not a perfect sphere,

⁵The water droplet at equilibrium is considered to be a spherical cap.

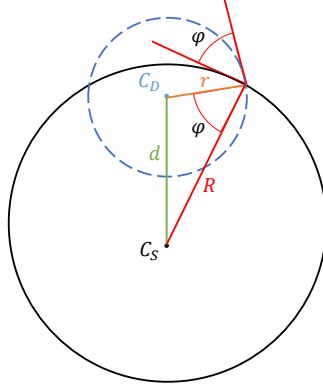


Figure 4: Illustration of the effective contact angle φ . C_S and C_D are the centers of solid particle sphere and drop water, respectively.

which explains the comparatively high error between θ and φ for the lowest value in Fig. 4.

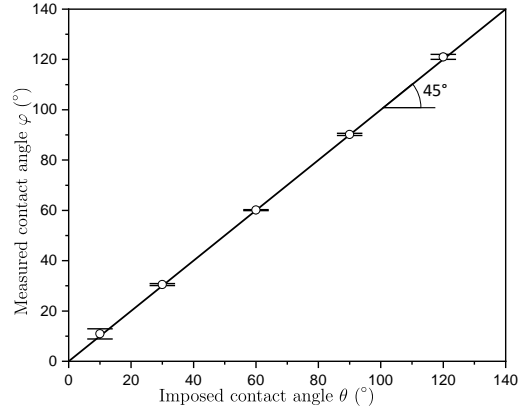


Figure 5: Measured versus imposed contact angles for a drop on a spherical particle. The solid line represents $f(\theta) = \theta$.

3.2. Capillary rise in a tube

The capillary rise benchmark is performed to validate the model. This benchmark consists of a tube with a radius r , which is placed vertically in a reservoir filled with a liquid subjected to gravity. Due to the capillarity effect in the tube, the liquid will rise to a certain height h (see Fig. 6). In the numerical setup, periodic BCs are applied on the left, right, front and back

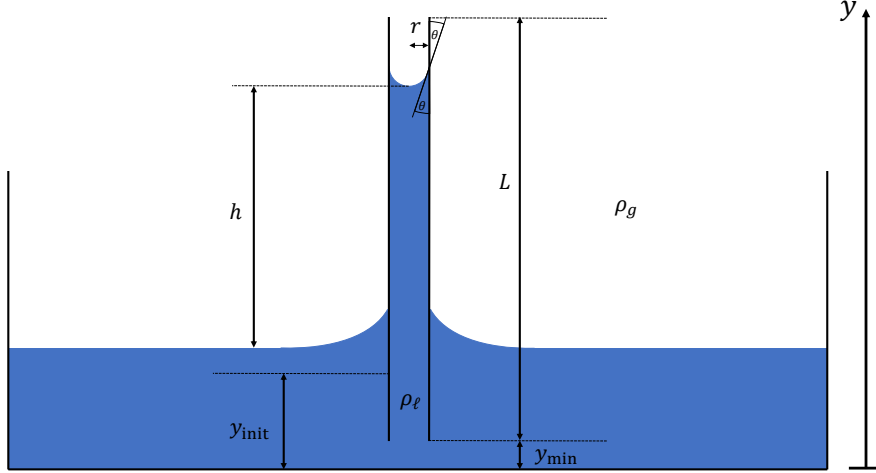


Figure 6: Side view schematic describing the capillary rise benchmark.

boundaries. Bounce-back and wetting condition are applied on the tube wall as well as on the top and bottom of the domain. The domain size is $N_x \times N_y \times N_z = 192 \times 224 \times 192$. The domain is initialized with the liquid film below $y_{\text{init}} = 80$ lu both inside and outside of the tube. This latter has a thickness of 3 lu, and a radius $r = 12$ lu. The minimum position of the tube is at $y_{\text{min}} = 15$ lu with a length $L = 185$ lu as shown in Fig. 6.

Jurin's law can be applied to find the height h of capillary rise at hydrostatic equilibrium

$$h = \frac{2\gamma \cos \theta}{\Delta\rho g r} \quad (38)$$

where $\Delta\rho = \rho_\ell - \rho_g$, r is the tube radius, γ is the surface tension, g is the gravity, and θ is the contact angle.

For a contact angle $\theta = 0^\circ$, h yields:

$$h = \frac{2\gamma}{\Delta\rho g r}. \quad (39)$$

The parameters for the real system and the simulation are shown in Table 1. According to Eq. (39), the expected capillary rise is $h = 9.8$ mm with $r = 1.5$ mm.

To simulate the capillary rise, conversion of units must be carried out to link physical to lattice units (c.f. Appendix A for more details). In the presence

of gravity, the conversion between gravity in lattice and physical units is given as:

$$g = \tilde{g} \frac{C_L}{C_T^2}. \quad (40)$$

After calculating C_T from (A.3), the gravity in lattice units can be deduced from (40) as:

$$\tilde{g} = g \frac{C_T^2}{C_L}. \quad (41)$$

The LBM measured height at equilibrium (as defined in Fig. 7) is $h = 10.06$ mm (80 lu) which is in a good agreement with the expected value of 9.8 mm (78 lu) with a relative error of 2.65 %.

It must be highlighted that another mesh size ($r = 4$ lu) was carried out to investigate its dependency on the LBM numerical results. Even though water could rise in the tube, an error of 32 % with respect to the expected theoretical height has been found.

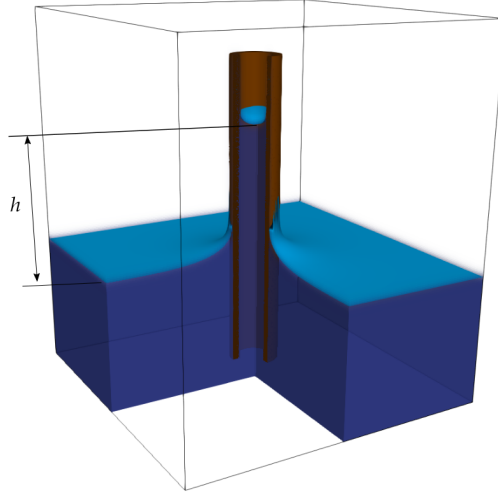


Figure 7: Capillary rise at equilibrium.

Quantities	Physical parameters	Value in SI units	Lattice parameters	Values in lattice units
Liquid density (water)	ρ_l	1000 kg/m ³	ρ^{lu}	1000
Gas density (air)	ρ_g	1 kg/m ³	ρ^{lu}	1
Characteristic length	r	1.5 mm	r^{lu}	12
Surface tension	γ	0.07213 N/m	γ^{lu}	0.2
Contact angle	θ	0°	θ	0°
Gravity	g	9.81 m/s ²	g^{lu}	4.25×10^{-7}
Expected capillary rise	h	9.82 mm	h^{lu}	78
Measured capillary rise	h	10.06 mm	h^{lu}	80

Table 1: Capillary rise parameters in physical and lattice units.

4. Capillary forces

After validating the model as well as the wetting condition through benchmarks, the capillary forces problem can be next tackled. In this section, we will see that the formulation of the Newtonian fluid is not sufficient for computing capillary forces. It is then necessary to include the adhesion term—asccribed to [Fisher \(1926\)](#)—in order to retrieve the experimental data. In this section, numerical method is presented to compute this supplementary term.

4.1. Capillary forces in a doublet from Young-Laplace equation

We recall the expression of Young-Laplace equation that gives the capillary bridge’s profile between two solid spherical particles ([Gagneux and Millet, 2014](#)). In the absence of gravity, Young-Laplace equation in the particular case of axisymmetric capillary bridges of revolution around x -axis classically writes as

$$\frac{y''(x)}{(1 + y'^2(x))^{3/2}} - \frac{1}{y(x)\sqrt{1 + y'^2(x)}} = -\frac{\Delta p}{\gamma} = H \quad (42)$$

where $H = -\frac{\Delta p}{\gamma}$ is the mean curvature, $\Delta p = p_{in} - p_{out}$ is the pressure difference between inside and outside of the capillary bridge, and γ is the surface tension of the fluid-gas system.

By integrating Young–Laplace equation over the bridge, the capillary force induced by the liquid bridge between two particles (see [Fig. 8](#)) can be calculated at the neck radius y^* as follows ([Gagneux and Millet, 2014](#)):

$$F^{\text{cap}} = \underbrace{-\Delta p \pi y^{*2}}_{F_p} + \underbrace{2\pi \gamma y^*}_{F_{ad}}. \quad (43)$$

Note that the capillary forces can be decomposed into two parts, a pressure force F_p and a surface tension force F_{ad} . As it is a first integral of Young–Laplace equation, the capillary force is constant at any point of the profile $y(x)$ and can also be calculated at the contact line by [Gagneux and Millet \(2014\)](#)

$$F^{\text{cap}} = \underbrace{-\Delta p \pi R^2 \sin^2 \delta}_{F_p} + \underbrace{2\pi \gamma R \sin \delta \sin(\delta + \theta)}_{F_{ad}} \quad (44)$$

where δ is the filling angle, and R is the radius of the particle. Moreover, for any position along the capillary bridge, we can write

$$F^{\text{cap}} = \underbrace{-\Delta p \pi y(x)^2}_{F_p} + \underbrace{2\pi \gamma y(x) \cos \psi}_{F_{ad}} \quad (45)$$

where $\psi(x)$ denotes the angle between the tangent of the profile at point $(x, y(x))$ and the horizontal axis as illustrated in Fig. 8.

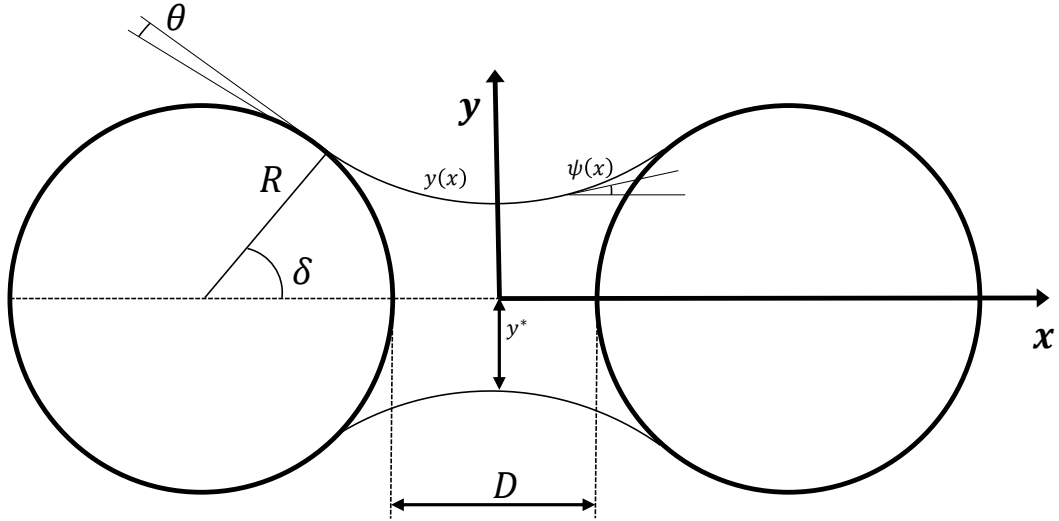


Figure 8: Capillary bridge profile between two spherical particles.

4.2. Forces exerted by the fluid on a solid

4.2.1. Classical case without interface

In a classical way, the force exerted by a fluid on a solid can be calculated based on the integration of the fluid stress tensor σ_f on a given surface Ω close to the particle as shown in Fig. 9. Thus,

$$\mathbf{F}_f = \int_{\Omega} \boldsymbol{\sigma}_f \cdot \mathbf{n}_{\Omega} dS \quad (46)$$

where \mathbf{n}_{Ω} is the outer unit normal vector to the surface Ω and dS is an elementary area element. The stress tensor $\boldsymbol{\sigma}_f$ for a Newtonian fluid is classically given by

$$\boldsymbol{\sigma}_f = -p\mathbf{I} + \boldsymbol{\tau} \quad (47)$$

where p is the fluid pressure, \mathbf{I} is the identity matrix in \mathbb{R}^3 , and $\boldsymbol{\tau}$ is the viscous stress tensor defined as

$$\boldsymbol{\tau} = 2\mu(\nabla\mathbf{u} + \nabla\mathbf{u}^T) \quad (48)$$

where μ is the dynamic fluid viscosity ($\mu = \rho\nu$) and \mathbf{u} the fluid velocity. Eq. (46) is valid when no discontinuity surfaces are intercepted by Ω . Con-

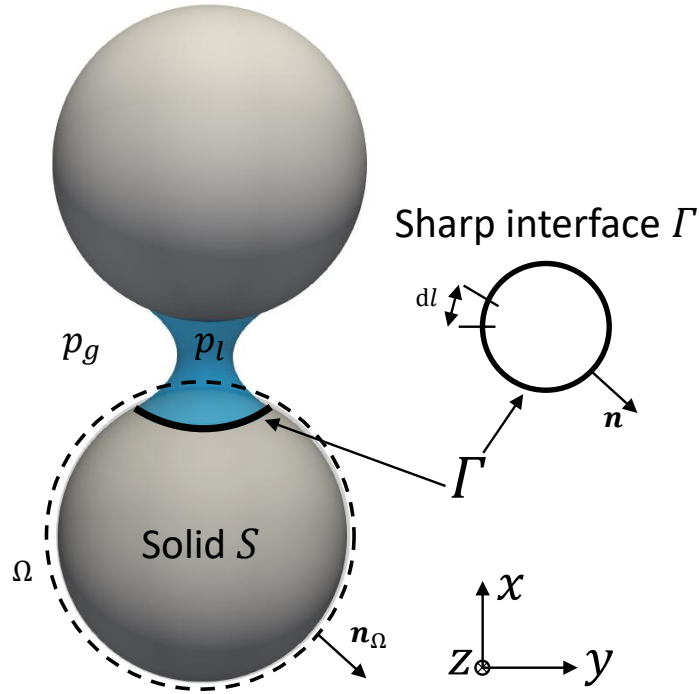


Figure 9: Capillary bridge and integration domain within a sharp interface.

trary to the theoretical framework, in our simulations, the interface is smooth,

so that we can integrate $\boldsymbol{\sigma}_f \cdot \mathbf{n}_\Omega$ on any Ω surface (no stress jump). Let us calculate the contribution (46) over the domain Ω surrounding the solid S (Fig. 9).

The domain Ω can be split into Ω_g and Ω_l ($\Omega = \Omega_g \cup \Omega_l$), where Ω_g and Ω_l are the gas and liquid domains⁶, respectively. From Eq. (46), we have

$$\mathbf{F}_f = \int_{\Omega_g} \boldsymbol{\sigma}_f \cdot \mathbf{n}_\Omega dS + \int_{\Omega_l} \boldsymbol{\sigma}_f \cdot \mathbf{n}_\Omega dS \quad (49)$$

and considering only the pressure term at equilibrium⁷ we get:

$$\mathbf{F}_f = \int_{\Omega_g} -p_g \mathbf{n}_\Omega dS + \int_{\Omega_l} -p_l \mathbf{n}_\Omega dS. \quad (50)$$

If we assume that p_g is constant, we can then write

$$\mathbf{F}_f = - \int_{\Omega_l} (p_l - p_g) \mathbf{n}_\Omega dS - \int_{\Omega} p_g \mathbf{n}_\Omega dS = - \int_{\Omega_l} \Delta p \mathbf{n}_\Omega dS \quad (51)$$

where Δp is the pressure difference between air and water. For negative values of Δp or positive value of the mean curvature H , that is the general case of stable nodoid configurations (Gagneux and Millet, 2014), we have an attractive capillary force. However, Eq. (51) involves only the Laplace pressure contribution leading to the first term F_p in Eqs. (43), (44) or 45 for the capillary force. A supplementary term must therefore be added to account for the adhesion term as previously presented in Eqs. (43), (44), and (45).

4.2.2. Capillary interface surface stress-like tensor

In the case of a sharp interface, the stress is not continuous in the fluid phase across the capillary interface and a supplementary term must be added in Eq. (47) (to enforce continuity in the normal stress vector) of the fluid stress to account for the adhesion term involved in Eq. (43). Therefore, we have to consider that

⁶The interface is defined at the isosurface $\phi = 0.5$. Above that value, we enter in the liquid domain Ω_l . And below $\phi = 0.5$, it will be the gas domain Ω_g as shown in Fig. 1b

⁷Because the macroscopic velocity \mathbf{u} will tend to 0 at equilibrium $\mathbf{u} \rightarrow \mathbf{0}$ (see Fig. 13 for more details)

$$\hat{\boldsymbol{\sigma}}_f = \begin{cases} \gamma \mathbf{I}_{T_w}, & \text{on the interface} \\ \boldsymbol{\sigma}_f & \text{otherwise} \end{cases} \quad (52)$$

where \mathbf{I}_{T_w} denotes the identity of the tangent plane of the capillary interface (see Fig. 10). It is worth noting that $\hat{\boldsymbol{\sigma}}_f$ is a 2D object on the interface and a 3D object in the bulk fluids. A similar stress-like tensor term has been added for describing the contribution of capillary interfaces in stress calculation in partially saturated medias (Duriez and Wan, 2017; Popinet, 2018; Scardovelli and Zaleski, 1999)

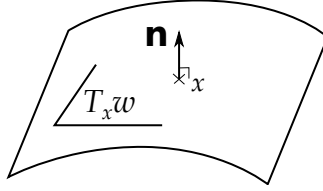


Figure 10: Sketch of an identity of the tangent plane.

The capillary force is therefore now expressed as

$$\hat{\mathbf{F}}_f = \int_{\Omega} \boldsymbol{\sigma}_f \mathbf{n}_{\Omega} dS + \int_{\Gamma} \gamma \mathbf{I}_{T_w} \cdot \mathbf{n}_{\Omega} dl \quad (53)$$

where Γ is the intersection of Ω with the capillary interface as shown in Fig. 9. Using the fact that $\mathbf{I}_{T_w} \cdot \mathbf{n}_{\Omega}$ is independent of ξ , and denoting $\mathbf{m} = (\mathbf{n} \times \mathbf{n}_{\Omega}) \times \mathbf{n}$, Eq. (53) yields to:

$$\hat{\mathbf{F}}_f = \int_{\Omega} \boldsymbol{\sigma}_f \mathbf{n}_{\Omega} dS + \gamma \int_{\Gamma} \mathbf{m} dl. \quad (54)$$

We have used the classical formula $\mathbf{I}_{T_w} \cdot \mathbf{n}_{\Omega} = \mathbf{n}_{\Omega} - (\mathbf{n}_{\Omega} \cdot \mathbf{n}) \cdot \mathbf{n} = (\mathbf{n} \times \mathbf{n}_{\Omega}) \times \mathbf{n}$, where \mathbf{n} denotes the normal to the interface as shown in Fig. 9. It is worth noting that the second term of $\hat{\mathbf{F}}_f$ in Eq. (54) corresponds to that mentioned in Connington et al. (2015a); Zhang et al. (2020) and Connington et al. (2015b). It is general and valid for a sharp interface (strong discontinuity). It is also worth mentioning that \mathbf{m} represents the unit tangent vector to the interface as illustrated in Fig. 14.

In the phase-field LBM model, however, the interface is defined with a thickness W as already seen in Fig. 1a. In that particular case, the interface

becomes a surface⁸ case as depicted in Fig. 11, instead of a contour in $\Omega \cap \Gamma$ as seen in Fig. 9, therefore Eq. (54) must be rewritten as follows

$$\hat{\mathbf{F}}_f = \int_{\Omega} \boldsymbol{\sigma}_f \mathbf{n}_{\Omega} dS + \gamma \int_{\Omega} \mathbf{m} \delta_s(\xi) dS \quad (55)$$

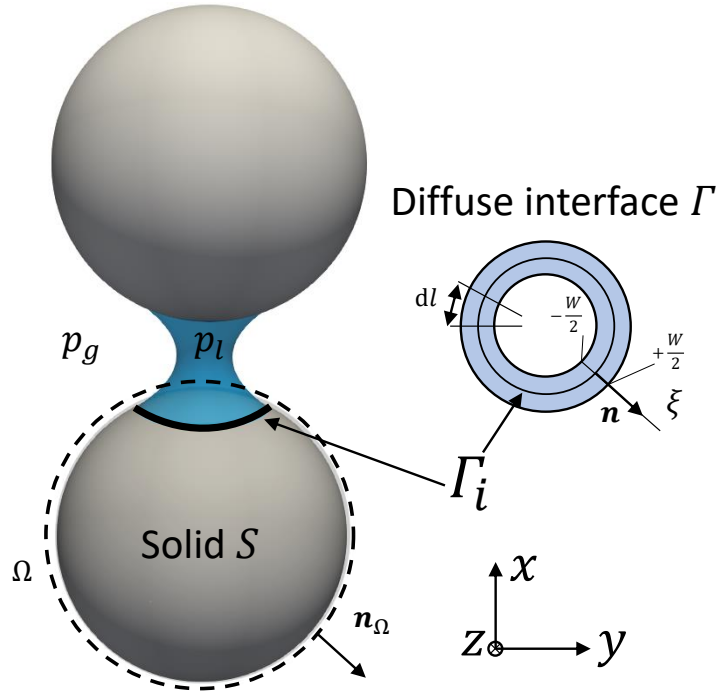


Figure 11: Capillary bridge and integration domain within a thick interface.

where $\delta_s(\xi)$ is the regularized Dirac function of the capillary interface defined along the thickness direction ξ (cf. Fig. 12)

$$\delta_s(\xi) = \frac{24}{W} \phi(\xi)^2 [\phi(\xi) - 1]^2 \quad (56)$$

⁸The surface becomes a set of multiple contours Γ_i . In other words, the interface becomes $= \bigcup_i \Gamma_i$

where $\phi(\xi)$ is function of ξ given by inverting Eq. (8) that satisfies the condition:

$$\int_{-\infty}^{+\infty} \delta_s(\xi) d\xi = 1. \quad (57)$$

PS: It is worthy to note that the second term of the right hand side of Eq.(55) would exactly be the same as the second term of Eq.(54) if one supposed that the interface were sharp (zero thickness). In the case of a sharp interface, the Dirac function would be the unit impulse Dirac as depicted in Fig. 12. In fact, the unit impulse Dirac function δ_s will transform the domain Ω into a contour Γ .

Obviously, the larger the width W is, the smoother the δ_s as illustrated in Fig.12. For all of the simulations in this paper " $W = 5$ lu" is chosen, which is suitable to make the Dirac function smooth enough to avoid numerical instabilities.

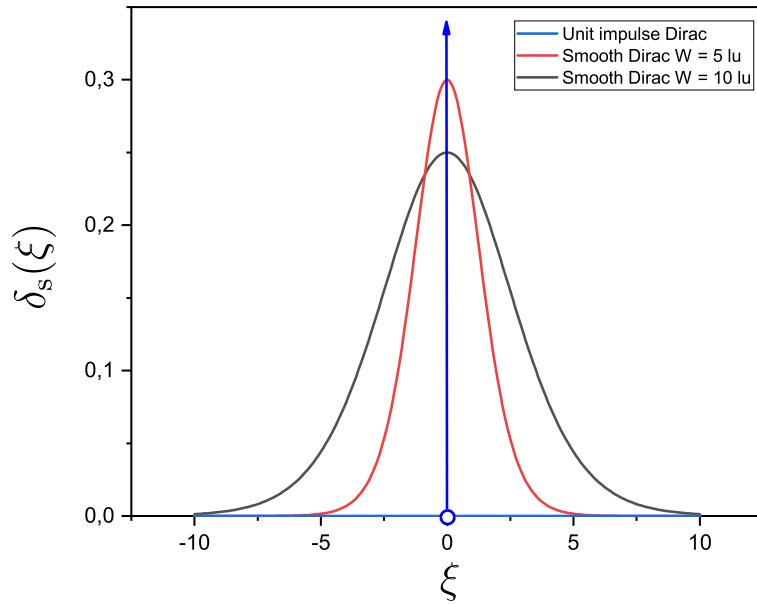


Figure 12: Smooth Dirac functions for $W \in \{5; 10\}$ lu as well as the unit impulse Dirac function.

As a consequence, the contribution of the second term of the right hand side of (55) leads to:

$$\mathbf{F}_\gamma = \gamma \int_{\Gamma_i} \left[\int_{-\infty}^{+\infty} \delta_s(\xi) d\xi \right] \mathbf{m} dl. \quad (58)$$

Using Eq. (56), as \mathbf{m} does not depend on ξ , the adhesion force \mathbf{F}_γ acting on Γ_i can be written as:

$$\mathbf{F}_\gamma = \frac{24\gamma}{W} \int_{\Gamma_i} \int_{-\infty}^{+\infty} \phi^2(\xi) [\phi(\xi) - 1]^2 \mathbf{m} d\xi dl. \quad (59)$$

The integral can be appropriately expressed with respect to the phase function ϕ . For this purpose, we take advantage of the inverse of Eq. (8) to express ξ as a function of ϕ :

$$\xi = \frac{W}{4} \ln \left(\frac{\phi}{1 - \phi} \right), \quad \phi \in [0; 1]. \quad (60)$$

Next, $d\xi$ can be explicitly transformed into $d\phi$ as:

$$d\xi = \frac{W}{4\phi(1 - \phi)} d\phi. \quad (61)$$

Then, by substituting Eq. (61) into (59), the expression of the adhesion force for diffuse interface can be derived:

$$\mathbf{F}_\gamma = -6\gamma \int_{\Gamma_i} \int_0^1 \phi(\phi - 1) \mathbf{m} d\phi dl. \quad (62)$$

4.3. Numerical LBM-based implementation

To evaluate numerically the force given in Eq. (55), a discrete form in terms of pressure contribution is required, i.e.;

$$\mathbf{F}_p = \sum_{\mathbf{x}_S} \boldsymbol{\sigma}_f \cdot \mathbf{n}_\Omega \Delta S. \quad (63)$$

Note that the sum runs over all lattice points \mathbf{x}_S located on the voxelated surface Ω , and the area element ΔS is equal 1 in lattice units. We define F_τ as the viscous force, resulting from the viscous stress tensor $\boldsymbol{\tau}$, as follows:

$$\mathbf{F}_\tau = \int_{\Omega} \boldsymbol{\tau} \cdot \mathbf{n}_\Omega dS \quad (64)$$

Once the capillary bridge is established, the macroscopic velocity \mathbf{u} will tend to zero. Consequently, according to Eq. (64), viscous forces \mathbf{F}_τ will also be nil. The x-component of viscous force F_τ^x is depicted in Fig. 13. It shows that the x-component will tend to zero at the equilibrium of the simulation⁹. Accordingly, viscous forces are not taken into consideration in the computation of capillary forces.

Technically speaking, in order to compute the viscous stress tensor $\boldsymbol{\tau}$, each node of LBM simulations in 3D conditions should contain 6 components¹⁰ $\{\tau_{\alpha\beta}\}$, where $\alpha, \beta \in \{x; y; z\}$. In fact, when using 16 GBs—which are the total amount of memory in the graphics card Quadro RTX 5000 used in this study—the declaration of these 6 variables for each node would cost roughly 2 GBs. Thus, from a technical point of view, it is advantageous to neglect the viscous force for memory optimization to provide a maximum performance.

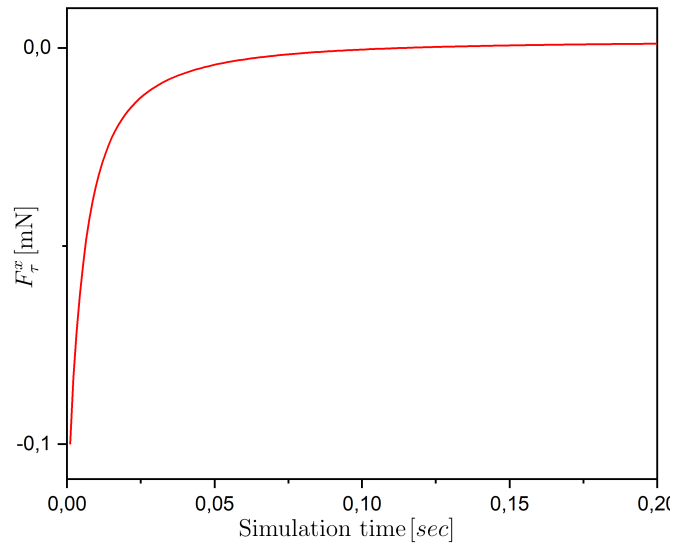


Figure 13: The x-component viscous force F_τ^x tends gradually to 0 when reaching equilibrium.

Alternatively, the total hydrodynamic forces acting on a given particle by the

⁹Since the capillary bridge is oriented along x-axis, as illustrated in Fig. 15, the y and z components of the viscous force F_τ^y and F_τ^z will automatically be zero from the beginning to the end of the simulation due to symmetry.

¹⁰Thanks to the symmetry of the tensor.

fluid can be calculated based on the momentum exchange algorithm proposed by Ladd (1994):

$$\mathbf{F}_{ME} = \sum_{\mathbf{x}_S} \sum_{\alpha} [f_{\alpha}^*(\mathbf{x}_b, t) + f_{\alpha}(\mathbf{x}_b, t + \Delta t)] \mathbf{c}_{\alpha}. \quad (65)$$

where \mathbf{x}_S are the same voxels used in Eq. (63).

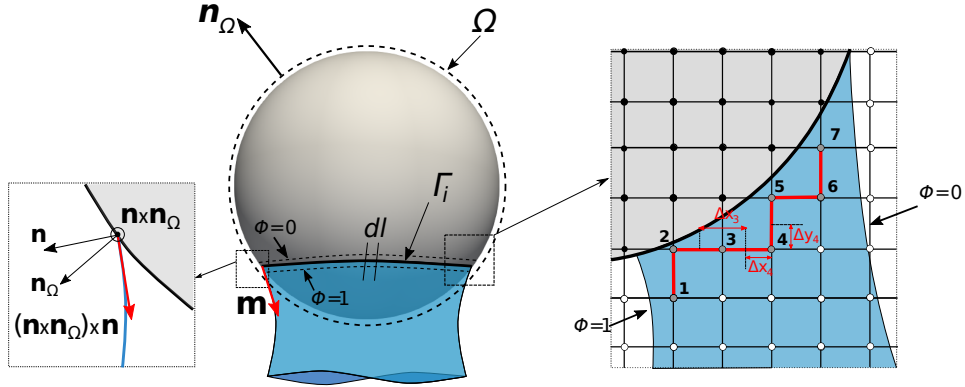


Figure 14: Schematic view of the contact line Γ_i on a spherical particle. dl is a line element on the contact line and \mathbf{m} represents the unit vector directed along the local capillary force. In the zoom, the live nodes (grey circles numbered from 1 to 7) used to calculate the capillary force along the width direction of a diffuse interface around a curved solid boundary. The white and black circles represent the fluid and solid nodes, respectively.

Expression (62) leads to the discrete form of the elementary adhesion force \mathbf{f}_{γ} along an element dl of Γ_i (with $dl = 1$ lu)

$$\mathbf{f}_{\gamma} \approx -6\gamma \sum_j \phi_j (\phi_j - 1) \mathbf{m}_j |\Delta\phi_j| \quad (66)$$

with

$$|\Delta\phi_j| = \left| \frac{\partial\phi}{\partial x} \right|_j |\Delta x_j| + \left| \frac{\partial\phi}{\partial y} \right|_j |\Delta y_j| + \left| \frac{\partial\phi}{\partial z} \right|_j |\Delta z_j| \quad (67)$$

We have noted $\left. \frac{\partial\phi}{\partial x} \right|_j$, $\left. \frac{\partial\phi}{\partial y} \right|_j$ and $\left. \frac{\partial\phi}{\partial z} \right|_j$ the local partial derivatives at the live node j , and Δx_j , Δy_j , and Δz_j the local coordinate increments in the x , y ,

and z directions, respectively. They can be computed as

$$\begin{cases} \Delta x_j = \sum_{k=1}^2 0.5\Psi(\mathbf{x}_j + \boldsymbol{\varepsilon}_k^x) \\ \Delta y_j = \sum_{k=1}^2 0.5\Psi(\mathbf{x}_j + \boldsymbol{\varepsilon}_k^y) \\ \Delta z_j = \sum_{k=1}^2 0.5\Psi(\mathbf{x}_j + \boldsymbol{\varepsilon}_k^z) \end{cases} \quad (68)$$

with the notations

$$\boldsymbol{\varepsilon}^x = [\boldsymbol{\varepsilon}_1^x, \boldsymbol{\varepsilon}_2^x] = \begin{bmatrix} 1 & -1 \\ 0 & 0 \\ 0 & 0 \end{bmatrix}, \quad \boldsymbol{\varepsilon}^y = [\boldsymbol{\varepsilon}_1^y, \boldsymbol{\varepsilon}_2^y] = \begin{bmatrix} 0 & 0 \\ 1 & -1 \\ 0 & 0 \end{bmatrix}, \quad \boldsymbol{\varepsilon}^z = [\boldsymbol{\varepsilon}_1^z, \boldsymbol{\varepsilon}_2^z] = \begin{bmatrix} 0 & 0 \\ 0 & 0 \\ 1 & -1 \end{bmatrix} \quad (69)$$

and

$$\Psi(\mathbf{x}) = \begin{cases} 0, & \text{if } \mathbf{x} \text{ is not a live node} \\ 1, & \text{if } \mathbf{x} \text{ is a live node} \end{cases} \quad (70)$$

Note that Eqs. (68)-(70) are compact notations that simplify the numerical implementation. Finally, the total surface tension force exerted on a particle can be obtained by

$$\mathbf{F}_\gamma = \sum_i \mathbf{f}_{ad} \approx -6\gamma \sum_i \sum_j \phi_j(\phi_j - 1) \mathbf{m}_j |\Delta\phi_j| \Delta l_i \text{ (lu)} \quad (71)$$

where the first sum runs over all the discrete line elements $\Delta l_i = 1 \text{ lu}$, while the second one runs over all live nodes in the i^{th} line element. Finally, the complete capillary force $\hat{\mathbf{F}}_f = \mathbf{F}_p + \mathbf{F}_\gamma$ may be calculated as follows using (63) and (71):

$$\hat{\mathbf{F}}_f \approx \sum_{\mathbf{x}_S} \boldsymbol{\sigma}_f \cdot \mathbf{n}_\Omega \Delta S - 6\gamma \sum_i \sum_j \phi_j(\phi_j - 1) \mathbf{m}_j |\Delta\phi_j| \Delta l_i \text{ (lu)} \quad (72)$$

5. Numerical examples

In this section, capillary forces will be computed for two and three spherical particle grains and compared to experimental and numerical data from [Mielniczuk et al. \(2018\)](#) and [Miot et al. \(2021\)](#), respectively. It is worth mentioning that all the simulations of capillary bridges—whether for doublets or triplets—are carried out in zero-gravity condition.

¹¹Gray or the numbered nodes in Fig. 14 are the so-called live nodes

5.1. Capillary bridge between two spherical particles

Capillary bridges between two spherical particles are simulated to validate the calculation of the associated capillary forces presented in Section 4. The simulations are carried out with a domain size of $N_x \times N_y \times N_z = 160 \times 250 \times 160$, with the particles having a radius of $R = 4$ mm. The characteristic length in the x-direction is $L_c = 12$ mm, therefore the mesh size $\Delta x = 0.012 / (N_x - 1) \approx 7.5 \times 10^{-5}$ m. A drop of water with a spherical shape is created at mid-distance between the two particles as illustrated in Fig. 15a; two different initialization setups are used with water volumes of 4 and 10 μL . Also, different separation distances $D \in \{0.5, 1, 1.5, 2, 2.25\}$ mm are considered. The contact angle $\theta = 20^\circ$ is imposed in the wetting condition (32). At the convergence of the LBM simulation as shown in Fig. 15b, the capillary forces are calculated at the Contact Line (CL) using Eq. (72). Fig. 16 shows the simulation results of the capillary forces F^{cap} for different separation distances D and for two distinct volumes: 4 and 10 μL . The experimental and numerical data of Mielniczuk et al. (2018) and Miot et al. (2021), respectively, are added for comparison. It can be seen that the simulation results are in a very good agreement with experimental as well as numerical data of Mielniczuk et al. (2018) and Miot et al. (2021), which validates the proposed approach, while also proving that Eq. (62) coincides with the adhesion term at contact line given by Eq. (44).

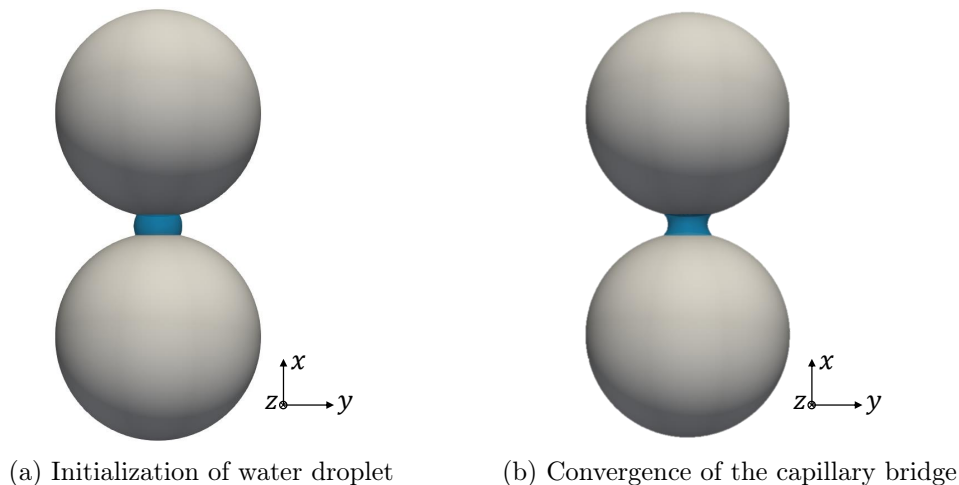


Figure 15: From initialization of water droplet at mid-distance to the convergence of the capillary bridge for a water volume of $V = 10 \mu\text{L}$ for $\theta = 20^\circ$.

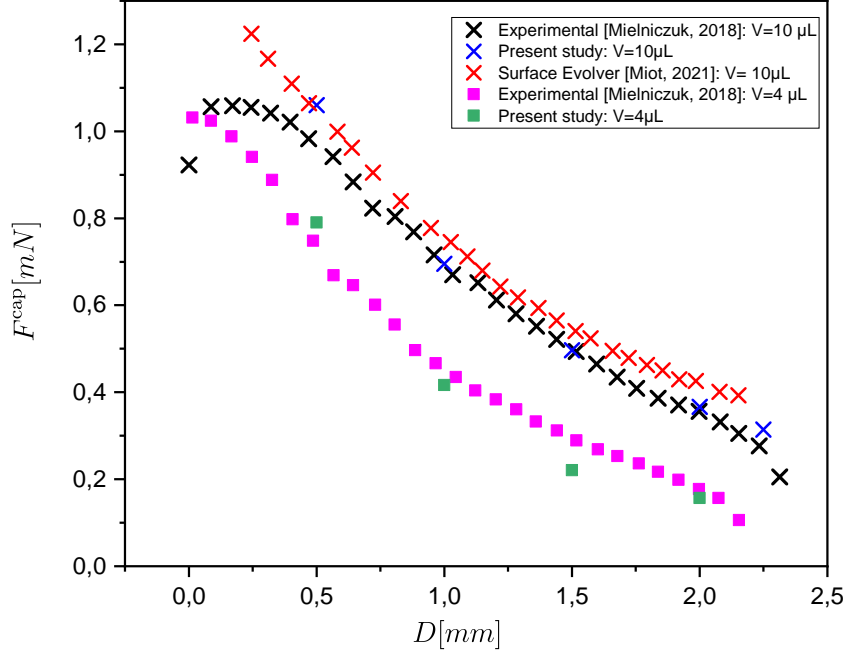


Figure 16: Capillary forces F^{cap} versus separation distances D for water volumes of 10 and 4 μL .

It must be noted that the convergence of capillary bridges is reached when the imposed contact angle θ is attained. However the question that arises is: what makes the imposed angle attainable? The answer will be summarized into three steps: (1) the initialization of water droplet where the interface velocities are 0, (2) whereupon the transition phase begins, during which water droplet starts moving outward at velocities of $\mathcal{O}(10^{-4})$ lu, (3) lastly the convergence where the interface velocities tend, theoretically, to 0 when the imposed contact angle θ is eventually reached. However, from a numerical point of view, at convergence, the order of magnitude of interface velocities are $\mathcal{O}(10^{-5})$ lu which are negligible with respect to that during the transition phase.

5.2. Capillary bridges between three spherical particles (coalescence)

Given that the numerical approach was validated with the case of a capillary doublet between two spherical particles, the challenge is to next explore capillary forces of three solid grains and, in particular, to the coalescence (merging) of the two menisci. The configuration used in [Miot et al. \(2021\)](#) is used to provide a comparison between LBM and energy minimization results altogether.

The triplet configuration is defined as following: the centers of the two bottom particles are separated by a distance $D_2 = 8.3$ mm. The upper particle is placed at a distance $D_1 = 8.7$ mm from the centers of the bottom particles as presented in [Fig. 17a](#). Note that the particles are in the same plane in z -direction. The particles are of the same radius $R = 4$ mm.

All the simulations are performed with the domain size of $N_x \times N_y \times N_z = 320 \times 320 \times 320$ nodes. The characteristic length considered is $L_c = 24$ mm in x -direction. Therefore, the mesh size chosen is $\Delta x = 0.024/(N_x - 1) \approx 7.5 \times 10^{-5}$ m. Two spherical water drops are initialized in the mid-segment between the top and the right bottom particle, and between the top and the left bottom particle as seen in [Fig. 17a](#). In this latter, where there is no contact between capillary bridges at any moment of the simulation, each capillary bridge will converge separately to its own equilibrium as shown in [Fig. 17b](#). However, when the water volume is sufficiently large as illustrated in [Fig. 18a](#), a contact between capillary bridges may probably take place at some point of the simulation¹² producing a merging (coalescence) between both capillary bridges as shown in [Fig. 18b](#). Once capillary bridges are coalesced, they will be treated as a single merged capillary bridge and will not converge until the imposed contact angle θ is respected—as seen in [Fig. 18c](#). A parametric study is performed by varying the initial water volume V and contact angle θ . The vertical capillary force exerted onto the upper particle is also computed from [Eq. \(72\)](#).

[Fig. 19](#) depicts the capillary force for different liquid volumes (from 1 to 33 μL) and different contact angles $\theta \in \{20^\circ, 40^\circ, 50^\circ\}$. The LBM simulations are performed without gravity so as to compare with those of [Miot et al. \(2021\)](#) carried out under the same conditions.

¹²When every single capillary bridge is converging to its own equilibrium until satisfying the imposed contact angle θ , contact lines of the both capillary bridges may touch.

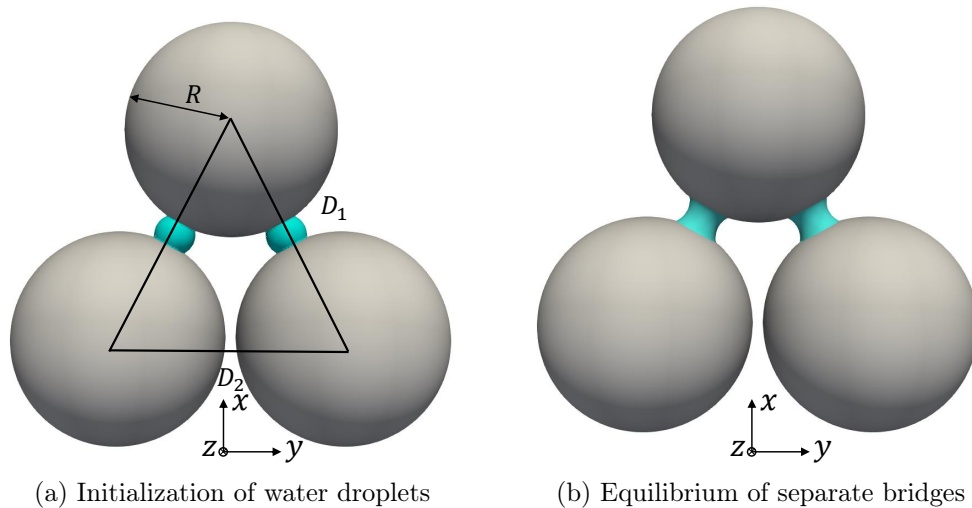


Figure 17: From initialization of two water droplets to the equilibrium of capillary bridges for a total water volume of $V = 3.5 \mu\text{L}$ for $\theta = 20^\circ$.

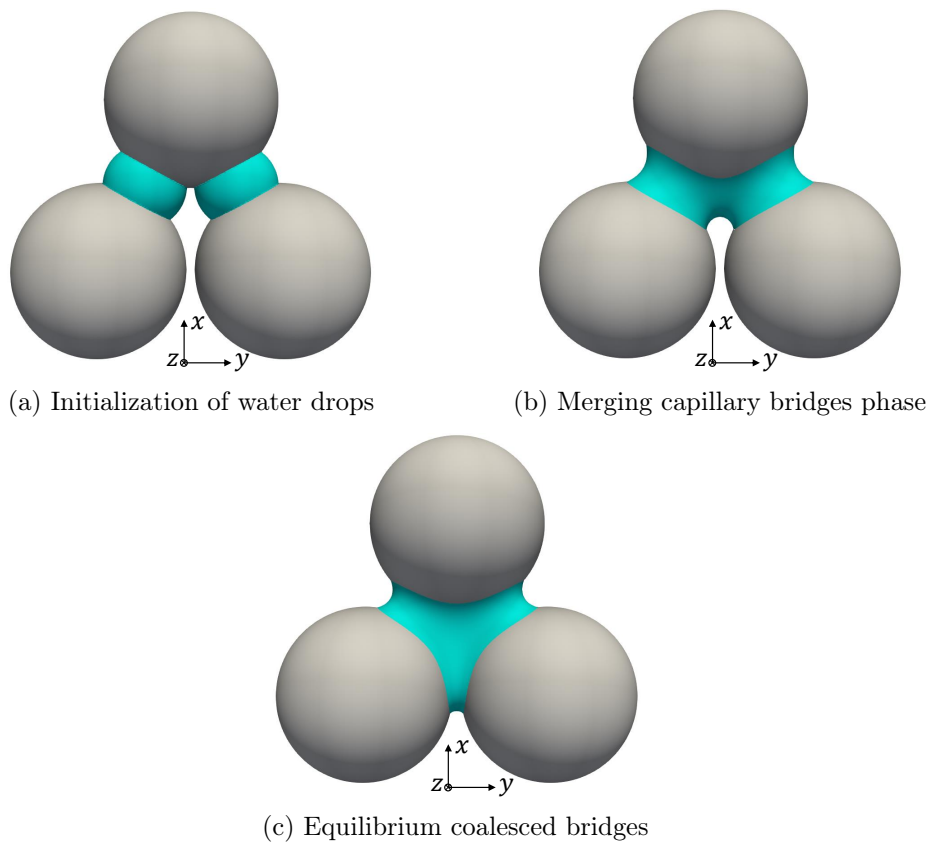


Figure 18: From initialization of two³¹ water drops to the equilibrium of coalesced capillary bridges for a total water volume of $V = 31.5 \mu\text{L}$ for $\theta = 20^\circ$.

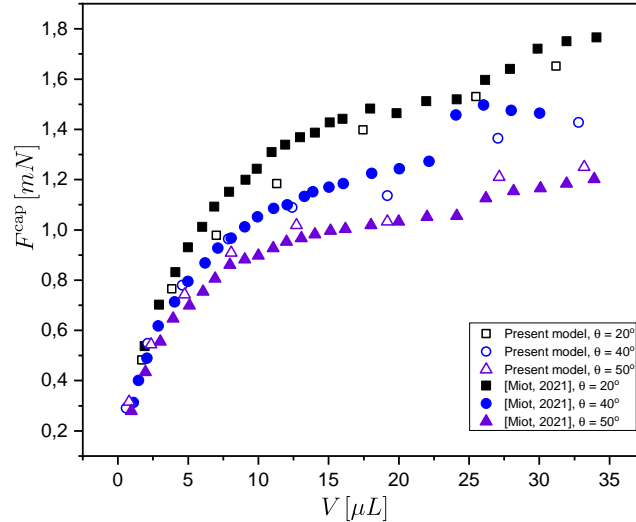


Figure 19: Comparison of the capillary forces F^{cap} , computed on the upper particle, between the present model (LBM simulations) and Surface Evolver used in Miot et al. (2021) for different volumes V [μL] and contact angles θ .

A rather good agreement can be noted between the results. Most importantly, the advantage of the present method is that the forces (adhesion, pressure, and viscous forces) are accessible at any time step, while in Miot et al. (2021) the total forces are calculated only at equilibrium using the Virtual Work Principle. Moreover, the most precious asset of the present model is that it can easily handle the dynamics of capillary bridges without needing to choose whether the bridges are coalesced or not in the first place (funicular or pendular regimes), which makes this model extremely powerful and promising for treating partially saturated granular assemblies. In addition to these features, the new geometric algorithm for computing capillary forces using Eq. (72) is proved to be applied on all types of capillary bridges regardless of their regime (coalesced or isolated capillary bridges).

6. Conclusion

In this paper, we proposed a diffuse-interface model based on Allen-Cahn equation within the LB solution of two-phase Navier-Stokes equation to capture capillary interfaces at solid grain boundaries. A surface tension term is added to Navier-Stokes equation to capture the physics of interphase surfaces.

Capillary forces then arise in the formulation and a numerical algorithm is developed that involves the integration of fluid pressure on a curved surface. A stress-like tensor term was added to take into account the discontinuity of the interface separating gas from liquid. In the case of a thick interface, the numerical scheme for computing this supplementary term was developed. The proposed model was successfully validated by two benchmarks that address the spreading of a liquid drop on a spherical particle and capillary rise in a tube. Besides capturing the geometry of the interfaces, the wetting conditions in terms of contact angle were also reproduced.

The predictive capabilities of the proposed model were further confirmed in two other examples that relate to a wet granular assembly. In a capillary doublet involving two equal-sized spherical particles, both the geometry of the intervening pendular liquid bridge and the associated capillary force agree well with experimental data. An extension to the case of three spherical particles where liquid bridges coalesce with a sudden increase in capillary force compares favourably with numerical results obtained using a surface energy minimization. The main feature of the proposed model is that the merging of capillary bridges is easily handled. Accordingly, future studies should address LBMxDEM (Discrete Element Method), where computed capillary forces—either from single or coalesced capillary bridges—will be added into DEM simulations in order to investigate in depth the behavior of thousands of grains when subjected to water for large degrees of saturation S_r . Furthermore, dynamic behavior of capillary bridges will also be addressed in future studies.

In closing, the model presented in this paper provides a viable numerical framework within which the dynamics of wetting following the various transitions of capillary regimes can be computed in a large assembly of arbitrarily shaped solid particles. Most importantly, associated capillary forces at the micro-/meso-scale can be calculated to evaluate their impact on both macroscopic strength and deformation of unsaturated granular media across all capillary regimes.

Acknowledgements

The authors would like to express their sincere gratitude to the Nouvelle-Aquitaine Region for funding the StabDigue project, to the IRN GeoMech network for their valuable discussions, and to the French National Centre for Space Studies (CNES) for having supported this work.

Appendix A. - Units Conversion

In LBM simulations, the mesh size and the time step are supposed to be equal to 1, i.e. $\Delta x_{\text{LBM}} = 1$ lattice unit (lu) and $\Delta t_{\text{LBM}} = 1$ lattice unit (lu) which are absolutely different from Δx_{Phy} and Δt_{Phy} . Consequently, other lattice units of LBM parameters will also follow. Therefore, a rescaling between physical and lattice units must be performed in order to make the simulations consistent with the physics, because all the LBM parameters are given in lu.

For the sake of simplicity, the following convention will be used: the subscripts 'LBM' and 'Phy' will be replaced by $\widetilde{\square}$ and nothing \square for lattice and physical units, respectively. For instance, $\Delta x_{\text{LBM}} = \widetilde{\Delta x}$ and $\Delta x_{\text{Phy}} = \Delta x$. The re-scaling of lengths, time, and densities are defined as follows

$$\Delta x = C_L \underbrace{\widetilde{\Delta x}}_{=1} \quad \Delta t = C_T \underbrace{\widetilde{\Delta t}}_{=1} \quad \rho = C_\rho \widetilde{\rho} \quad (\text{A.1})$$

where the units involved are respectively meters (m), seconds (s), and kg/m^3 . Eq. (A.1) gives the so-called canonical conversion factors. The first step to determine the conversion coefficient of any given physical parameter is to link its unit to the canonical aforementioned ones. For instance, the unit of surface tension γ becomes:

$$[\gamma] = \text{N} \cdot \text{m}^{-1} = \overbrace{\text{kg} \cdot \text{m} \cdot \text{s}^{-2}}^{\text{N}} \cdot \text{m}^{-1} = \frac{\text{kg}}{\text{m}^3} \cdot \text{m}^3 \cdot \text{s}^{-2} = C_\rho \cdot \frac{C_L^3}{C_T^2}. \quad (\text{A.2})$$

Thus, the conversion between surface tension γ in lattice and physical units yields to:

$$\gamma = \underbrace{C_\rho \frac{C_L^3}{C_T^2}}_{C_\gamma} \widetilde{\gamma}. \quad (\text{A.3})$$

References

- Benseghier, Z., Millet, O., Younes, N., 2021. A relevant phase-field-based lattice-boltzmann method for water-air capillary interfaces. Submitted to *Journal of Computational Physics* .
- Brakke, K.A., 1992. The surface evolver. *Experimental mathematics* 1, 141–165.
- Chiu, P.H., Lin, Y.T., 2011. A conservative phase field method for solving incompressible two-phase flows. *Journal of Computational Physics* 230, 185–204.
- Connington, K.W., Lee, T., Morris, J.F., 2015a. Interaction of fluid interfaces with immersed solid particles using the lattice boltzmann method for liquid–gas–particle systems. *Journal of Computational Physics* 283, 453–477.
- Connington, K.W., Miskin, M.Z., Lee, T., Jaeger, H.M., Morris, J.F., 2015b. Lattice boltzmann simulations of particle-laden liquid bridges: Effects of volume fraction and wettability. *International Journal of Multiphase Flow* 76, 32–46.
- Di Renzo, A., Picarelli, G., Di Maio, F.P., 2020. Numerical investigation of funicular liquid bridge interactions between spherical particles. *Chemical Engineering & Technology* 43, 830–837.
- Dörmann, M., Schmid, H.J., 2017. Distance-dependency of capillary bridges in thermodynamic equilibrium. *Powder technology* 312, 175–183.
- Duriez, J., Wan, R., 2017. Contact angle mechanical influence in wet granular soils. *Acta Geotechnica* 12, 67–83.
- Fakhari, A., Bolster, D., 2017. Diffuse interface modeling of three-phase contact line dynamics on curved boundaries: A lattice boltzmann model for large density and viscosity ratios. *Journal of Computational Physics* 334, 620–638.
- Fakhari, A., Lee, T., 2013. Multiple-relaxation-time lattice boltzmann method for immiscible fluids at high reynolds numbers. *Physical Review E* 87, 023304.

- Fakhari, A., Mitchell, T., Leonardi, C., Bolster, D., 2017a. Improved locality of the phase-field lattice-boltzmann model for immiscible fluids at high density ratios. *Phys. Rev. E* 96, 053301.
- Fakhari, A., Mitchell, T., Leonardi, C., Bolster, D., 2017b. Improved locality of the phase-field lattice-boltzmann model for immiscible fluids at high density ratios. *Physical Review E* 96, 053301.
- Fakhari, A., Rahimian, M.H., 2010. Phase-field modeling by the method of lattice boltzmann equations. *Physical Review E* 81, 036707.
- Fisher, R., 1926. On the capillary forces in an ideal soil; correction of formulae given by w b haines. *The Journal of Agricultural Science* 16, 492–505.
- Gagneux, G., Millet, O., 2014. Analytic calculation of capillary bridge properties deduced as an inverse problem from experimental data. *Transport in Porous Media* 105, 117–139.
- Grof, Z., Lawrence, C.J., Štěpánek, F., 2008. The strength of liquid bridges in random granular materials. *Journal of Colloid and Interface Science* 319, 182–192.
- Hartmann, M., Palzer, S., 2011. Caking of amorphous powders—material aspects, modelling and applications. *Powder Technology* 206, 112–121.
- He, Q., Li, Y., Huang, W., Hu, Y., Wang, Y., 2019. Phase-field-based lattice boltzmann model for liquid-gas-solid flow. *Physical Review E* 100, 033314.
- Hornbaker, D., Albert, R., Albert, I., Barabási, A.L., Schiffer, P., 1997. What keeps sandcastles standing? *Nature* 387, 765–765.
- Huang, J., Shu, C., Chew, Y., 2009. Mobility-dependent bifurcations in capillarity-driven two-phase fluid systems by using a lattice boltzmann phase-field model. *International journal for numerical methods in fluids* 60, 203–225.
- Jacqmin, D., 1999. Calculation of two-phase navier–stokes flows using phase-field modeling. *Journal of Computational Physics* 155, 96–127.
- Krueger, T., Kusumaatmaja, H., Kuzmin, A., Shardt, O., Silva, G., Viggen, E., 2016. *The Lattice Boltzmann Method: Principles and Practice*. Graduate Texts in Physics, Springer.

- Ladd, A.J., 1994. Numerical Simulations of Particulate Suspensions Via a Discretized Boltzmann Equation. Part 1. Theoretical Foundation. *Journal of Fluid Mechanics* 271, 285–309.
- Lee, H.G., Kim, J., 2012. An efficient and accurate numerical algorithm for the vector-valued allen–cahn equations. *Computer Physics Communications* 183, 2107–2115.
- Lee, T., Liu, L., 2010. Lattice boltzmann simulations of micron-scale drop impact on dry surfaces. *Journal of Computational Physics* 229, 8045–8063.
- Li, Q., Yu, Y., Luo, K.H., 2019. Implementation of contact angles in pseudopotential lattice boltzmann simulations with curved boundaries. *Phys. Rev. E* 100, 053313.
- Li, X., Dong, M., Zhang, H., Li, S., Shang, Y., 2020. Effect of surface roughness on capillary force during particle-wall impactation under different humidity conditions. *Powder Technology* 371, 244–255.
- Liang, H., Liu, H., Chai, Z., Shi, B., 2019. Lattice boltzmann method for contact-line motion of binary fluids with high density ratio. *Phys. Rev. E* 99, 063306.
- Liang, H., Xu, J., Chen, J., Wang, H., Chai, Z., Shi, B., 2018. Phase-field-based lattice boltzmann modeling of large-density-ratio two-phase flows. *Phys. Rev. E* 97, 033309.
- Lievano, D., Velankar, S., McCarthy, J.J., 2017. The rupture force of liquid bridges in two and three particle systems. *Powder Technology* 313, 18–26.
- Liu, H.R., Ding, H., 2015. A diffuse-interface immersed-boundary method for two-dimensional simulation of flows with moving contact lines on curved substrates. *Journal of Computational Physics* 294, 484–502.
- Liu, H.R., Gao, P., Ding, H., 2017. Fluid–structure interaction involving dynamic wetting: 2d modeling and simulations. *Journal of Computational Physics* 348, 45–65.
- Liu, P., Yang, R., Yu, A., 2013. Dem study of the transverse mixing of wet particles in rotating drums. *Chemical Engineering Science* 86, 99–107.

- Louati, H., Oulahna, D., de Ryck, A., 2017. Effect of the particle size and the liquid content on the shear behaviour of wet granular material. *Powder Technology* 315, 398–409.
- Lu, N., Wu, B., Tan, C.P., 2007. Tensile strength characteristics of unsaturated sands. *Journal of Geotechnical and Geoenvironmental Engineering* 133, 144–154.
- Mielniczuk, B., Hueckel, T., El Youssoufi, M.S., 2015. Laplace pressure evolution and four instabilities in evaporating two-grain liquid bridges. *Powder Technology* 283, 137–151.
- Mielniczuk, B., Millet, O., Gagneux, G., El Youssoufi, M.S., 2018. Characterisation of pendular capillary bridges derived from experimental data using inverse problem method. *Granular Matter* 20, 14.
- Miot, M., Veylon, G., Wautier, A., Philippe, P., Nicot, F., Jamin, F., 2021. Numerical analysis of capillary bridges and coalescence in a triplet of spheres. *Granular Matter* 23, 1–18.
- Nguyen, H.N.G., Millet, O., Gagneux, G., 2019a. Exact calculation of axisymmetric capillary bridge properties between two unequal-sized spherical particles. *Mathematics and Mechanics of Solids* 24, 2767–2784.
- Nguyen, H.N.G., Millet, O., Gagneux, G., 2019b. Liquid bridges between a sphere and a plane-classification of meniscus profiles for unknown capillary pressure. *Mathematics and Mechanics of Solids* 24, 3042–3060.
- Nguyen, H.N.G., Millet, O., Gagneux, G., 2019c. On the capillary bridge between spherical particles of unequal size: analytical and experimental approaches. *Continuum Mechanics and Thermodynamics* 31, 225–237.
- Nguyen, H.N.G., Millet, O., Gagneux, G., 2019d. On the capillary bridge between spherical particles of unequal size: analytical and experimental approaches. *Continuum Mechanics and Thermodynamics* 31, 225–237.
- Nguyen, H.N.G., Millet, O., Zhao, C.F., Gagneux, G., 2020a. Theoretical and experimental study of capillary bridges between two parallel planes. *European Journal of Environmental and Civil Engineering* , 1–11.

- Nguyen, H.N.G., Zhao, C.F., Millet, O., Gagneux, G., 2020b. An original method for measuring liquid surface tension from capillary bridges between two equal-sized spherical particles. *Powder Technology* 363, 349–359.
- Nguyen, H.N.G., Zhao, C.F., Millet, O., Selvadurai, A., 2021. Effects of surface roughness on liquid bridge capillarity and droplet wetting. *Powder Technology* 378, 487–496.
- Penrose, O., Fife, P.C., 1990. Thermodynamically consistent models of phase-field type for the kinetic of phase transitions. *Physica D: Nonlinear Phenomena* 43, 44–62.
- Popinet, S., 2018. Numerical models of surface tension. *Annual Review of Fluid Mechanics* 50, 49–75.
- Richefeu, V., El Youssoufi, M.S., Azéma, E., Radjai, F., 2009. Force transmission in dry and wet granular media. *Powder Technology* 190, 258–263.
- Scardovelli, R., Zaleski, S., 1999. Direct numerical simulation of free-surface and interfacial flow. *Annual review of fluid mechanics* 31, 567–603.
- Stratford, K., Adhikari, R., Pagonabarraga, I., Desplat, J.C., 2005. Lattice boltzmann for binary fluids with suspended colloids. *Journal of Statistical Physics* 121, 163–178.
- Sun, X., Sakai, M., 2016. Direct numerical simulation of gas-solid-liquid flows with capillary effects: An application to liquid bridge forces between spherical particles. *Phys. Rev. E* 94, 063301.
- Sun, Y., Beckermann, C., 2007. Sharp interface tracking using the phase-field equation. *Journal of Computational Physics* 220, 626–653.
- Wang, H., Chai, Z., Shi, B., Liang, H., 2016. Comparative study of the lattice boltzmann models for allen-cahn and cahn-hilliard equations. *Physical Review E* 94, 033304.
- Wang, H., Yuan, X., Liang, H., Chai, Z., Shi, B., 2019. A brief review of the phase-field-based lattice boltzmann method for multiphase flows. *Capillarity* 2, 33–52.

- Wang, J.P., Gallo, E., François, B., Gabrieli, F., Lambert, P., 2017a. Capillary force and rupture of funicular liquid bridges between three spherical bodies. *Powder Technology* 305, 89–98.
- Wang, J.P., Gallo, E., François, B., Gabrieli, F., Lambert, P., 2017b. Capillary force and rupture of funicular liquid bridges between three spherical bodies. *Powder Technology* 305, 89–98.
- Wu, D., Zhou, P., Wang, G., Zhao, B., Howes, T., Chen, W., 2020. Modeling of capillary force between particles with unequal contact angle. *Powder Technology* 376, 390–397.
- Zhang, X., Liu, H., Zhang, J., 2020. A new capillary force model implemented in lattice boltzmann method for gas–liquid–solid three-phase flows. *Physics of Fluids* 32, 103301.
- Zhao, C.F., Kruyt, N.P., Millet, O., 2019. Capillary bridges between unequal-sized spherical particles: Rupture distances and capillary forces. *Powder technology* 346, 462–476.
- Zheng, L., Zheng, S., Zhai, Q., 2015. Lattice boltzmann equation method for the cahn-hilliard equation. *Physical Review E* 91, 013309.